Asynchronous Shake-Table Testing of Seismic Resilient Multispan Bridges Having Buckling Restrained Braces in Bidirectional Ductile Diaphragm

Homero Carrion-Cabrera, M.ASCE[1]; and Michel Bruneau, Dist.M.ASCE[2]

Abstract: The bidirectional ductile end diaphragm concept uses energy-dissipating buckling restrained braces (BRB) as fuses located at the end of a bridge superstructure's floating spans. This system using BRBs can provide seismic resilient and damage-free bridges fully operational immediately after an earthquake. A shake-table testing program was conducted to subject a 1/2.5-scale specimen to series of ground motions. The specimen tested represents one span of a five-span bridge having BRBs connected to the abutment and the pier next to it. The purpose of these tests was to experimentally validate proposed connection details when subjected to the three-dimensional (3D) displacement histories (compared with the axis of the BRBs) that resulted from bidirectional ground motions and the fact that the connections must accommodate inclined BRB layouts. The test protocol included earthquake displacement histories that represent design demands, cycles of thermal excitations, and (to eventually make the BRBs fail) extreme motions. The testing program validated the effectiveness of the proposed concept and the ability of BRBs to sustain multiple ground motions before failure. **DOI: 10.1061/JSENDH.STENG-12845.**
© 2024 American Society of Civil Engineers.

Introduction

Current state of practice in seismic design of ordinary multispan bridges generally relies either on plastic hinging of columns to dissipate earthquake energy, or on base isolation. The first one implies damage to the gravity-carrying columns; the second one requires special bearings and expansion joints to accommodate displacements that can be extremely large in many cases. Using the bidirectional ductile end diaphragm concept with inexpensive buckling restrained braces (BRBs) can provide resilient bridges with damage-free columns at low cost while minimizing displacements demands to levels that can be easily accommodated. The elimination of bridge closures and repairs following earthquakes can prevent massive economic losses [for example, Enke et al. (2008) estimated partial indirect losses of $703 million, in addition to direct losses, due to bridge damage alone for an earthquake scenario in St. Louis].

BRBs are special braces capable to yield in axial tension and compression. They are nowadays widely used and design requirements for buckling restrained braced frames are specified by the AISC *Seismic Provisions for Structural Steel Buildings* (AISC 2022). In bridges, there have been many fewer applications to date. Examples include the Vincent Thomas Bridge (CoreBrace 2021; Ingham et al. 1997; Lanning et al. 2016a, b) and the Minato bridge (Kanaji et al. 2005), which were retrofitted with BRBs. Although these were large bridges, there can also be benefits in using BRBs to enhance the seismic performance of common bridges.

One concept developed for use in such common bridges is ductile end diaphragms, which consists of hysteretic devices (or structural fuses) implemented in the diaphragms located at the ends of spans. These ductile end diaphragms are intended to dissipate seismic energy and prevent damage in the substructure by limiting the magnitude of transmitted forces. The concept was initially developed and tested with various hysteretic devices for seismic forces in the transverse direction by Zahrai and Bruneau (1999a, b), and a design procedure provided by Alfawakhiri and Bruneau (2001) has been implemented in AASHTO (2011). Further shake-table studies by Carden et al. (2006) verified the concept by exciting, in their transverse direction, scaled bridges having BRBs as fuse elements at their end diaphragms. Later, the concept was expanded to bidirectional seismic forces for bridges with stiff structures (Celik and Bruneau 2009; Wei and Bruneau 2018). Carrion-Cabrera and Bruneau (2022a, b) analytically demonstrated that the system can be effective in multispan simply supported bridges. It remained to demonstrate experimentally that that BRBs can be effectively used in this concept.

Toward that purpose, shake-table experiments using two tables were conducted to evaluate and validate the behavior of bridge spans having bidirectional ductile end diaphragms equipped with BRBs as structural fuse elements. More specifically, the testing program sought to evaluate the performance of the system for different configurations of the bidirectional ductile end diaphragm, using different types of connections between the BRBs and superstructure, and between the BRBs and concrete supports (i.e., abutments). In particular, this testing investigated the ability of these connections to allow the BRBs to perform as intended while accommodating the three-dimensional (3D) relative displacements that develop during the seismic response. Finally, testing also allowed the experimentally obtained demand ductilities to be compared with results obtained from numerical analysis. Results of tests on a span having two different BRB configurations and different BRB connections are presented here.

[1]Bridge Engineer, Kiewit Infrastructure Engineering, 1687 114th Ave. SE Suite 210, Bellevue, WA 98004 (corresponding author). ORCID: https://orcid.org/0000-0001-6335-2060. Email: homerofe@buffalo.edu

[2]SUNY Distinguished Professor, Dept. of Civil Structural and Environmental Engineering, Univ. at Buffalo, Buffalo, NY 14260. ORCID: https://orcid.org/0000-0003-1170-468X. Email: bruneau@buffalo.edu

Note. This manuscript was submitted on June 1, 2023; approved on January 2, 2024; published online on April 22, 2024. Discussion period open until September 22, 2024; separate discussions must be submitted for individual papers. This paper is part of the ***Journal of Structural Engineering***, © ASCE, ISSN 0733-9445.

Selection of the Prototype and Specimen

The specimen chosen represents the first span of a prototype bridge (i.e., connected to an abutment at one end and to a pier at the other end). The bridge was a straight bridge with multiple simply supported floating spans, each span supported on bidirectional slider bearings having negligible stiffness and strength to resist horizontal deformations. Bearings at the ends of the bridge were considered to rest above abutments, and all intermediate bearings were seated on piers. The prototype bridge was designed to limit superstructure displacements and dissipate seismic energy such that piers or bents remain elastic.

Also, considering that the prototype and corresponding specimen are related by the laws of similitude (Harris and Sabnis 1999), design constraints were added to account for the fact that geometry, weight, and loads obtained from the prototype should be able to be replicated in the specimen within the limits of the testing facilities of the Structural Engineering and Earthquake Simulation Laboratory at the University at Buffalo (UB SEESL). Therefore, after several analysis and design iterations to generate realistic and acceptable bridges geometries and ductile end diaphragms, the resulting prototype selected was a five-span bridge with 30.48 m (100 ft) long spans and bent heights varying from 4.877 m (16 ft) to 5.486 m (18 ft) [i.e., 3.048 m (10 ft) to 3.656 m (12 ft) columns plus 1.829 m (6 ft) height of the cap] as shown in Figs. 1(a and b). The superstructure of this bridge was designed in compliance with the AASHTO *LRFD Bridge Design Specifications* (AASHTO 2017). It consists of four built-up girders 1,695.5 mm (66 and 3/4 in.) deep, having 279.4 mm (11 in.) $\times$ 41.3 mm (1 and 5/8 in.) flanges, and 15.9 mm (5/8 in.) web thickness, separated 4,572 mm (15 ft) between each other, and working as a composite section with a 231.8 mm (9 and 1/8 in.)] thick concrete slab. The final weight of the span was estimated equal to 20.98 MN (972 kips). Spans are supported on bents, each having three 1,371.6 mm(54 in.) $\times$ 1,219.2 mm(48 in.) columns with equal height, as shown in Fig. 1(b). Spans transfer vertical loads to their supports through flat sliding bearings.

From this prototype, the specimen to be tested had a scale of 1/2.5 and assumed a model with a 1.0 factor for gravity scaling. This scaling results in 2.5 times smaller dimensions, $(2.5)^2$ smaller areas, 2.5 bigger accelerations, and a time scale compressed by 2.5, and materials properties of the specimen had the same properties as the prototype. The specimen represents Span 1 in Fig. 1(a), where only the part of the superstructure with the ductile end diaphragm and its connection to concrete is modeled, as shown in Fig. 1(b). Girders in the specimen are W690 $\times$ 125 (W27 $\times$ 84) shape, with a 678 mm (26.7 in.) depth, spaced 1,829 mm (6 ft) (per direct scaling of the girder depth and spacing in the prototype). The bent cap and abutment are represented by concrete blocks, each one of them connected to a different shake table. The shake tables reproduced scaled acceleration and displacement histories obtained from the analytical model at the bent cap and abutment, respectively. A schematic of this concept for the specimen is shown in Fig. 1(c), where the abutment is the west shake table and the pier cap is the east shake table.

The yielding core areas of the BRBs were determined using a simplified equivalent lateral force (ELF) design method developed as part of this project, described by Carrion-Cabrera and Bruneau (2023) and summarized in the Appendix. In applying this procedure, for calculating stiffness, bents were assumed as cantilever columns (fixed at their base) in the longitudinal direction, and in the transverse direction, bent caps and foundation were considered as rigid. Furthermore, the design spectrum for Memphis, Tennessee (Fig. 2), was selected for design for consistency with previous work (Carrion-Cabrera and Bruneau 2022a, b; Wei and Bruneau 2016). The spectrum was adjusted in amplitude based on limits of the testing facilities and to limit the required BRB cross section area to at least 0.5 in^2 in each configuration. Here, 322.6 mm^2 (0.5 sq in.) was considered here to be the smallest cross-section area that can be manufactured to have a good BRB performance in a cyclic test.

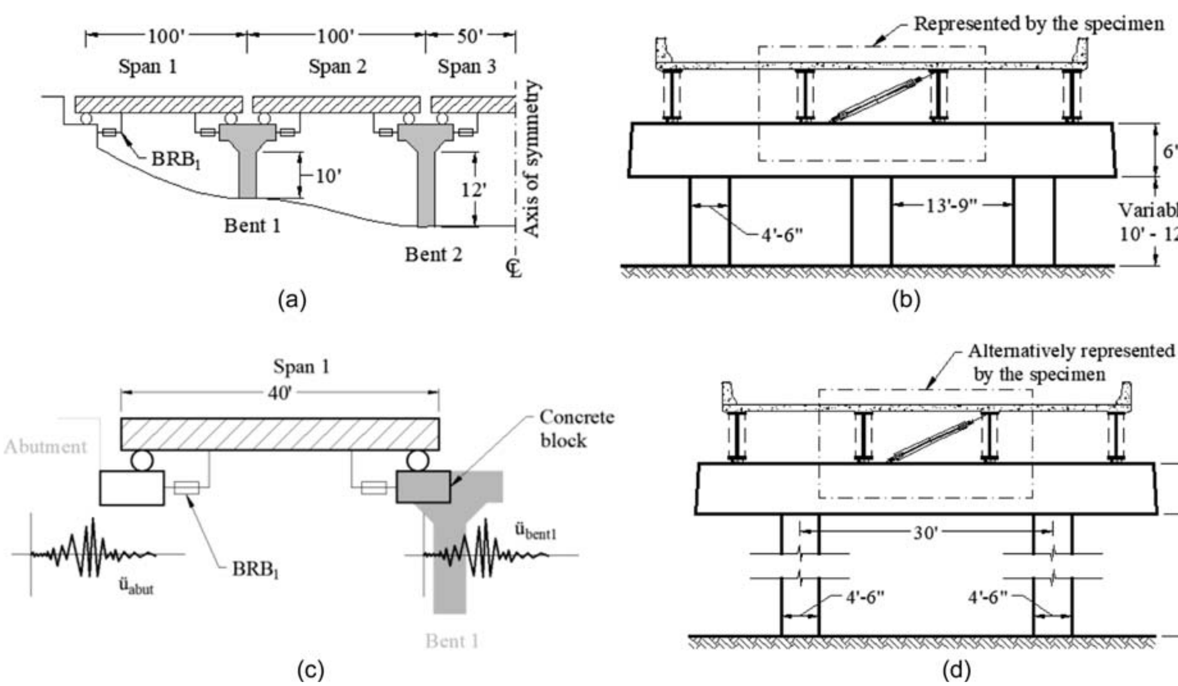

Fig. 1. Prototype: (a) scheme in the longitudinal direction; (b) geometry in the transversal direction; (c) model of the shake-table test; and (d) alternative considered.

© ASCE

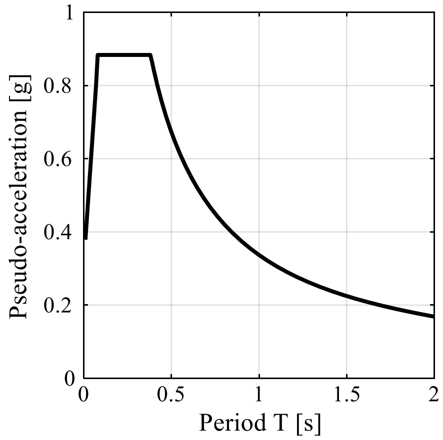

Fig. 2. Design spectrum.

The short bents in the bridge prototype were selected to meet the two experimental constraints: (1) the BRBs in the specimen needed to have a yielding cross-section area of at least 322.6 mm^2 (0.5 sq in.), and (2) accelerations obtained at the top of the bent cap (for the set of ground motions scaled to the design spectrum) needed to be smaller than the maximum acceleration that can be provided by the shake table. Nevertheless, a bridge with taller bents, shown in Fig. 1(d), was also analyzed as a candidate for prototype. It also showed good performance of the ductile end diaphragms with BRBs designed per the simplified methods, but it was not selected for testing because accelerations at the pier cap level were larger than could be applied by the shake table. In both bridges, the superstructure was the same as described previously.

BRB Configurations

BRBs in a bidirectional ductile end diaphragm and connecting the superstructure with the substructure can be provided in different configurations as long as the strength and stiffness provided by the group of BRBs in the longitudinal and transverse directions are in compliance with the design requirements. This provides for much flexibility in design and detailing. For that reason, two BRB configurations for the prototype bridges were analyzed and considered as possible candidates to be used in the specimen to be tested.

Both configurations presented here considered one end of the BRB connected to the abutment or bent cap while the other end was connected to the superstructure. The first configuration (named Configuration I here) considers a BRB in the transverse direction that connects to the superstructure at a point close to the top flange of the girder, whereas BRBs in the longitudinal direction are installed horizontally, as shown in Fig. 3(a). The advantage of this configuration is that the longitudinal BRBs can be connected directly to the girders bottom flanges and are almost horizontal. The second configuration tested (called Configuration II) is a modified version of Configuration I where the longitudinal BRBs are connected close to the top flange of the girder, as shown in Fig. 3(b). The advantage of this configuration is that the BRBs in the longitudinal direction are nested between the girders and thus protected from possible vehicle impacts. In both configurations, connections of slanted BRBs are subjected to rotations about two orthogonal axes.

As a result of using two configurations, the BRB cross-section areas of the yield core varied. For both configurations, at each end, only one BRB was used in the longitudinal direction. For Configuration I, BRBs in the transverse direction required a cross-section area equal to 322.6 mm^2 (0.5 sq in.), and in the longitudinal direction, 387.1 mm^2 (0.60 sq in.) and 322.6 mm^2 (0.50 sq in.) for BRBs connected to the abutment and to the bent cap, respectively. For BRB Configuration II, BRBs in the transverse direction required a cross-section area equal to 322.6 mm^2 (0.50 sq in.), and; in the longitudinal direction 451.6 mm^2 (0.70 sq in.) and 374.2 mm^2 (0.58 sq in.) for BRBs connected to the abutment and to the bent cap, respectively. For both BRB configurations, the period of the specimen in the transverse and longitudinal direction was 0.09 and 0.10 s, respectively, and for the entire bridge the period in the transverse and longitudinal direction was 0.10 and 0.18 s, respectively.

Connection of BRB to Girder

In some cases, connections of BRBs used in bidirectional ductile diaphragms may have special requirements compared with the connections typically used for BRBs in braced frames. This is because the connection used with BRBs in some of the configurations considered here must be able to allow rotation in two orthogonal directions. For instance, for the BRB shown in Fig. 4, the local axes in the connection (where all axes are perpendicular to each other) can be defined as follows: y is parallel to the longitudinal axis of the brace, z is in the vertical plane at the end of the span (plane shown in Fig. 4), and x is parallel to the longitudinal direction of the bridge (normal to the plane shown in Fig. 4). BRB connection rotations generated in a seismic event are expected to develop around the axes x and z when the span moves in the transverse and longitudinal direction, respectively.

To address rotation in two orthogonal directions, three types of BRB connections were considered to be used in the experiment. One of them was used previously in the seismic retrofit of the city hall of Vancouver, Canada, and featured on a CoreBrace (2020) website, and one was a standard pinned connection featured on a CoreBrace (2020) website, and one was developed and proposed

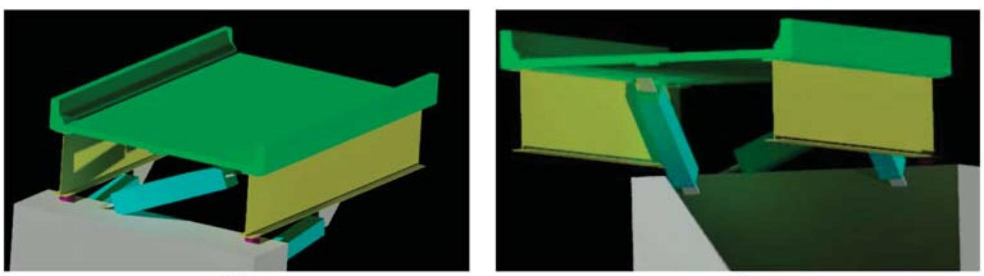

(a) (b)

Fig. 3. BRB configurations: (a) Configuration I; and (b) Configuration II.

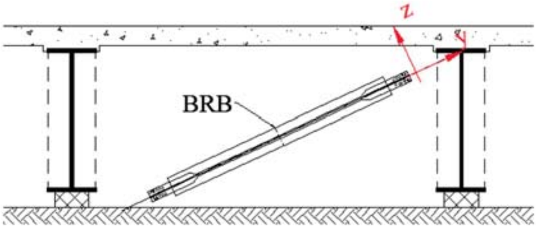

Fig. 4. Rotations in BRB-to-girder connection in transverse direction.

by the authors. The detail of the connection used in the Vancouver, Canada, city hall provides rotation around the z-axis by plastic bending of the gusset plate [shaded area shown in Fig. 5(a)], and around the x-direction by elastic bending of end plates in their strong axis and due to bolt slippage (oversized holes are not required and were not used to provide the needed rotation capacity; actually, standard hole diameters were used in this connection, and no sliding occurred during the test, as will be mentioned subsequently). Alternatively, the set of bolts could be substituted by a single pin, as shown in Fig. 5(b).

The fourth connection, shown in Fig. 5(c) and referred here as a universal connection, resulted from the merging of two connection concepts that have been previously used in concentrically braced frames, such as to provide rotational capacity by plastic bending in the shaded areas shown in Fig. 5(c). This connection is made by using a gusset plate orthogonal to the end plate from the BRB. For the detail shown in the figure, both plates are welded; however, a bolted connection option with four angles was proposed instead for easier BRB replacement during the testing program. All connections were designed taking into account stability concept from previous published papers (MacRae et al. 2021; Takeuchi et al. 2014; Zaboli et al. 2018). The BRB manufacturer was aware of this issue and claimed their standard connections are designed taking this into account. The connections developed by the authors were also designed to be stable while simultaneously reaching their maximum compressive axial force and expected maximum out-of-plane drifts.

Connection of BRB to Concrete

This section presents details on different connection concepts that were used to transfer forces from the BRBs to the span supports (e.g., abutment or bent cap). Moreover, because bidirectional ductile end diaphragms can be implemented both in existing bridges and in new bridges, here, connections that can be either postinstalled or cast-in place in concrete were both studied. Initially, connections with a base plate and postinstalled anchors using injectable adhesive were analyzed as a possible solution, but it was found that this strategy required an inordinately large number of anchors and considerable space for the case of BRBs in the longitudinal direction (because they transfer large tensile forces), so it was deemed to be unpractical for those BRBs. Instead, this concept was considered for the case of BRBs in the transverse direction because the tensile force transferred through the connection is the smallest. Because this connection uses postinstalled elements, it could be used as a retrofit solution.

Additionally, three other connection configurations were studied: one for retrofitting and two for new construction. The first uses a base plate with a 203.2 mm (8 in.) long, 38.1 mm (1.5 in.) wide, and 25.4 mm (1 in.) thick shear lug connected with four 19.1 mm (3/4 in.) diameter rods, F1554 Grade 105 steel (with yield strength equal to 724 MPa), and pretensioned to an anchor plate on the back concrete face, as shown in Fig. 6(a). A variation of this connection

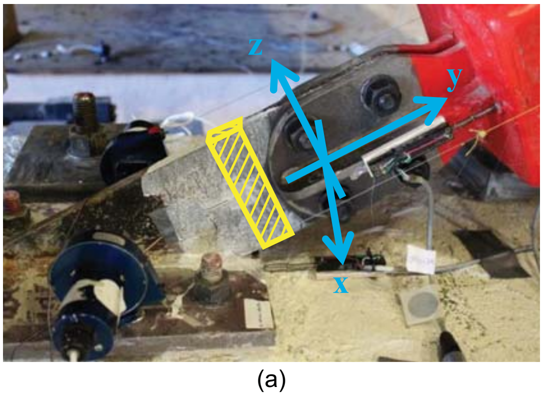

(a)

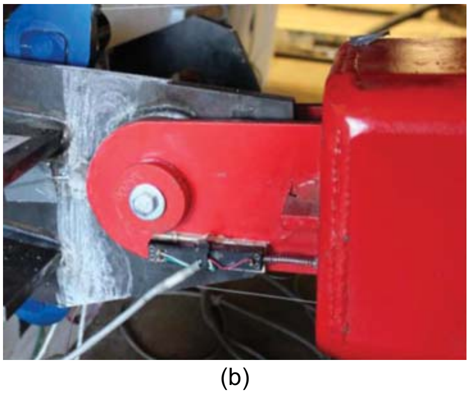

(b)

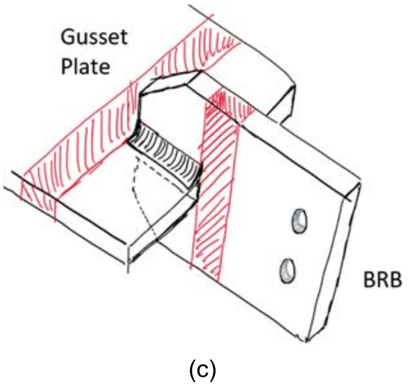

(c)

Fig. 5. BRB-to-girder connections: (a) with bolted connection; (b) with pinned connection; and (c) universal connection.

J. Struct. Eng., 2024, 150(7): 04024063

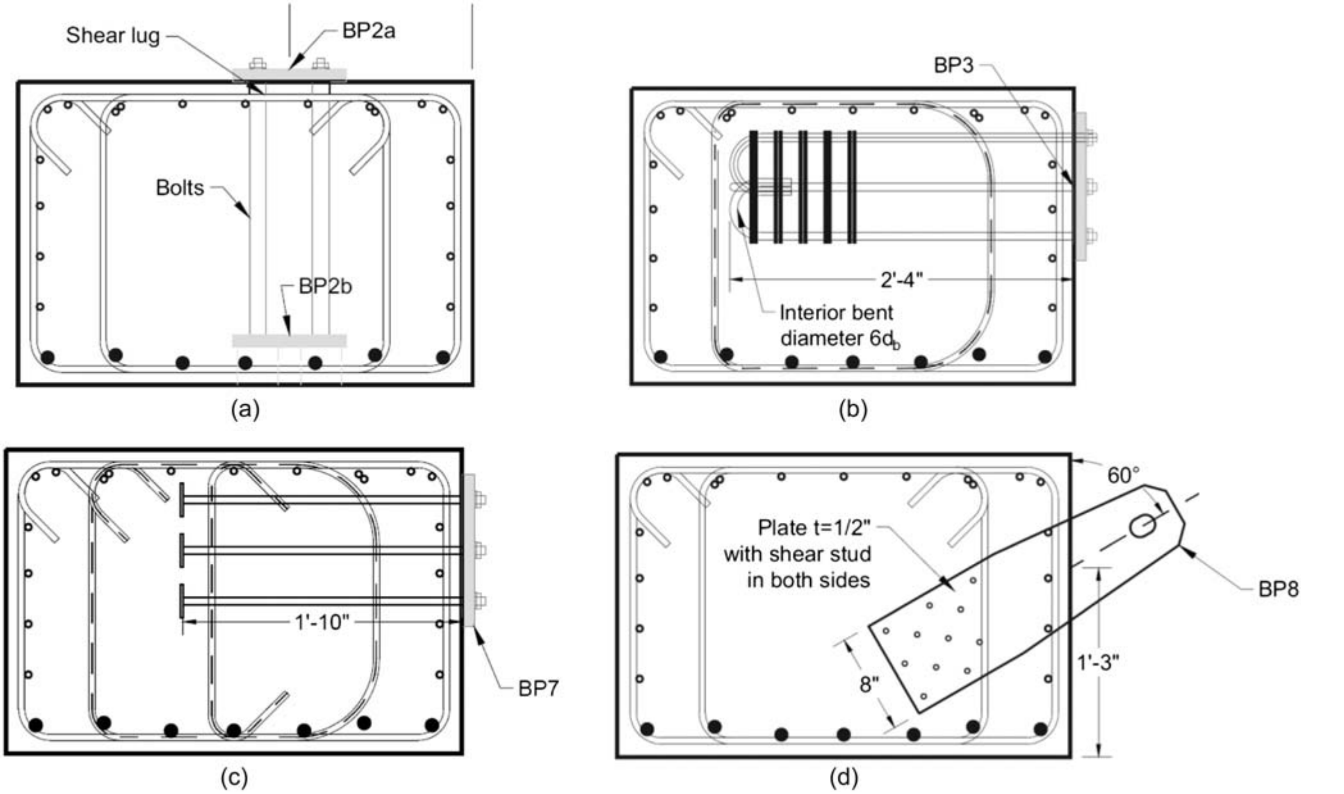

Fig. 6. Connection to concrete with (a) pretensioned rods; (b) J-hooked anchors; (c) threaded bars with nuts and washer; and (d) embedded steel shape. $1' = 1$ ft $= 304.8$ mm, and $1'' = 1$ in. $= 25.4$ mm.

with six 19.1 mm (3/4 in.) diameter threaded bars, F1554 Grade 105 steel, and without shear lug was also used.

The second one uses a base plate without shear lug and six 19.1 mm (3/4 in.) diameter J-hooked bolts, F1554 Grade 105 steel, embedded in the concrete with additional stirrups to ensure anchorage, and pretensioned, as shown in Fig. 6(b). A variation to this connection, shown in Fig. 6(c), uses six 19.1 mm (3/4 in.) diameter threaded bars, F1554 Grade 105 steel, embedded in concrete with nuts and washers at their ends as a mechanical anchor, and pretensioned [the detail in Figs. 6(b and c) was designed based on a strut and tie model, and the anchor design requirements in American Concrete Institute (ACI) standard ACI 318 (ACI 2019)].

The third one uses an embedded steel plate with studs welded in both sides as shown in Fig. 6(d) [this detail was also designed based on a strut and tie model, the anchor design requirements in ACI 318 (ACI 2019), and also the stud design requirements from AISC 360 (AISC 2016)]. Slight modifications to the presented concepts were used for the different BRBs in the two configurations. In total, five different connections between BRBs and concrete blocks (the substructure) were used in testing.

Design of Load Transfer from Slab to BRB

The inertia forces generated in the bridge superstructure in a seismic event mainly comes from the mass of the concrete deck. In the transverse direction, that force needs to be transferred to the ductile end diaphragms to be resisted by the BRBs. An adequate load path from the slab to the diaphragm must therefore be established. Here, a steel element with welded shear studs was designed to transfer an inertia force equal to (per capacity design principles) yielding and strain hardening of the BRBs of the ductile end diaphragms. In each end diaphragm, 11 studs with 9.5 mm (3/8 in.) diameters and 54 mm (2 and 1/8 in.) long were designed to be welded along the flange of a WT64 × 14.05 (WT2.5 × 9.5) shape located between girders in the transverse end diaphragm, as shown in Fig. 7. This detail is similar to one that has been developed by Carden et al. (2008).

In the longitudinal direction, two different details were used to transfer inertia forces to BRBs, one for each configuration. In Configuration I, forces from the concrete deck need to be transferred to the girder to be later resisted by BRBs. Here, similar to what was done in the transverse direction, capacity design was used to design studs welded on the girders of the specimen to directly transfer this inertia forces from the slab to the girders to ensure yielding in the BRBs connected to girders. In each girder, 16 studs with 9.5 mm (3/8 in.) diameters and 54 mm (2 and 1/8 in.) long were designed, to be welded equally spaced along the span.

In Configuration II, forces from the concrete deck need to be transferred to a steel plate with welded studs to be later resisted by the horizontal component of BRBs. The vertical component of the BRBs was transferred to the girders through a vertical plate stiffener and a common diaphragm to avoid a punching shear failure in the slab. Capacity design was used to design studs welded to the steel plate and the diaphragm to ensure yielding in the BRBs connected to the steel plate. In each steel plate, 23 studs with 9.5 mm (3/8 in.) diameters and 54 mm (2 and 1/8 in.) long were designed. Two slightly different details were used at each end of the span. In one end, the steel plate was also welded in one side to the girder flange, and at the other end, the steel plate was not welded to the flange and spaced 25.4 mm (1 in.) from it. Fig. 7(b) shows a conceptual view for Configuration II showing the studs in the girder and the steel plate.

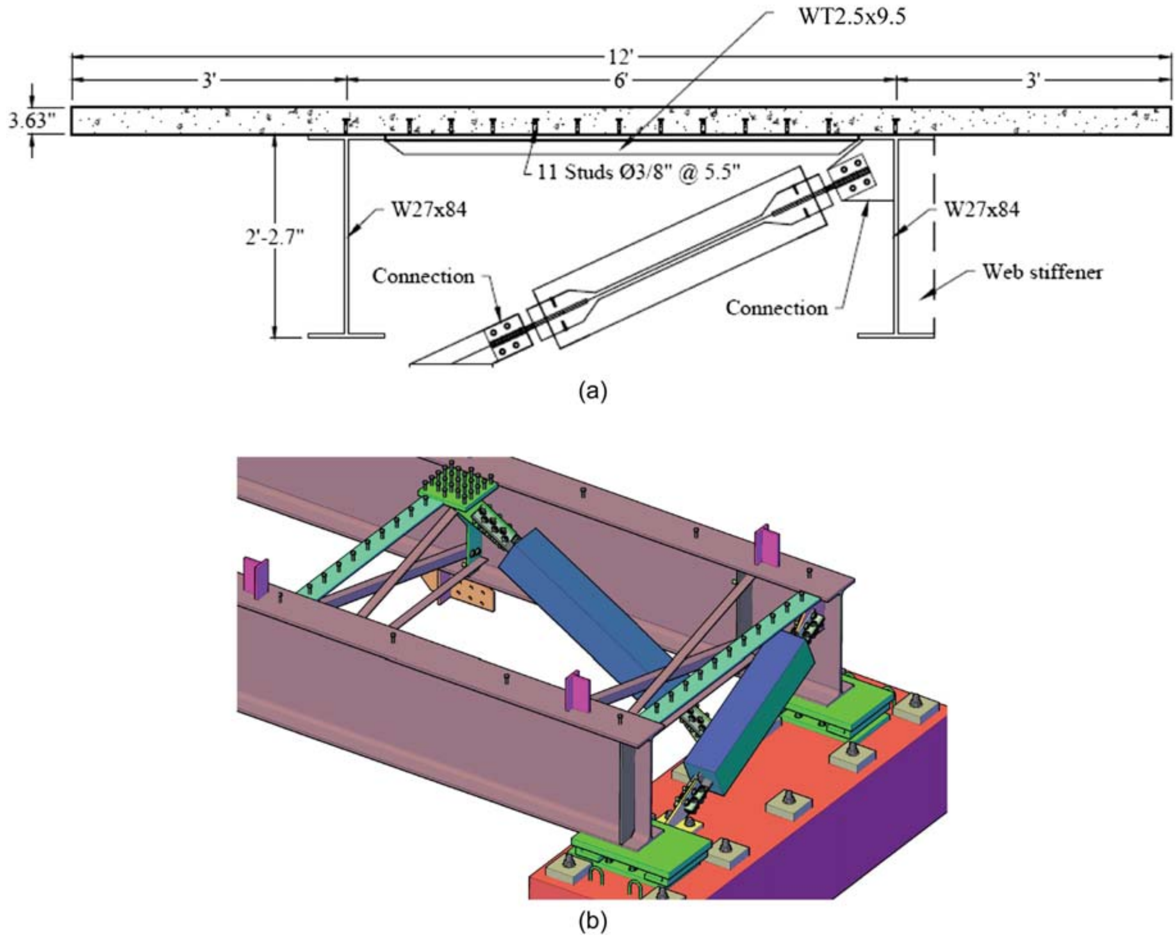

Fig. 7. (a) Studs in the transverse end diaphragm; and (b) conceptual view of Configuration II showing load transfer from slab to BRBs. $1' = 1$ ft $= 304.8$ mm, and $1'' = 1$ in $= 25.4$ mm.

Other Issues

Because BRBs connected at end diaphragms take care of resisting the seismic forces, cross-frames are only needed to brace the girders and avoid instabilities at the construction stage. As such, two L51 $\times$ 51 $\times$ 6.4 (L2 $\times$ 2 $\times$ 1/4) in an X configuration were used, spaced 3,048 mm (10 ft) between each other, which corresponds to a typical 7,620 mm (25 ft) spacing in the prototype. The test setup was designed based on plastic analysis and capacity design principles considering that BRBs in the specimen reach their maximum probable force. After the bridge specimen was designed up to a 60% level, feedback was collected from the BRB and bearing manufacturers to be able to progress further.

At that point, prior to building the entire bridge specimen, to ensure adequate behavior of BRBs with only a 322.6 mm^2 (0.5 sq in.) core area (never tested by the supplier before) and to obtain the strain hardening parameters needed for capacity design of the rest of the structure, two such BRBs were designed and shipped to the University of Buffalo where they were tested to cyclic deformations of up to $20\Delta_y$ for one BRB and $25\Delta_y$ for the other [the specimens used for this prequalification test were fabricated with steel having a measured yield strength equal to 263 MPa (38.1 ksi)]. This provided satisfactory evidence of axial ductile performance and strain hardening data needed to finalize production.

In production, by error, only some of the BRBs were fabricated using the same steel as that of the BRBs during qualification testing. The error was discovered prior to shipping. As a result, a second set of BRBs were produced and shipped to the UB SEESL in a separate batch. The BRBs in that second batch were stronger than the first ones because those BRBs were produced with a plate having a higher measured yield strength of 365 MPa (52.9 ksi). Two BRBs from this second batch were used as the BRBs in the transverse direction in Configuration II. The design spectrum was adjusted accordingly resulting in 0.85% and 0.92% the original spectrum for Configuration I and II, respectively.

Likewise, interaction with the bearing supplier led to revision in design and geometry, including an increase in height of the bearing that requires small modifications of all the BRB connection details accordingly. After being manufactured, the bearings were tested under static loads (at small velocities). Because the bearings were also designed to provide an uplifting resistance to resist tension forces at the support resulting from the specific layout of BRBs in the specimen and the reduction in mass resulting from the scaling process, bearings were tested under both compression and tension. The resulting friction coefficients obtained were 0.008 and 0.09 in compression and tension, respectively. Considering the weight of the specimen [1,360 kN (63 kips)], the lateral load needed to initiate sliding at each support (i.e., abutment or pier) was 5.4 kN (0.25 kips), which is equal to 1.5% of the horizontal projection of the yielding force of the weakest BRB [362.6 kN (16.8 kips)], and thus negligible.

At that point, final design was completed, and the specimen was built by a national steel fabricator and shipped to the University at Buffalo's laboratory for testing.

Instrumentation Plan and Loading Protocol

During testing, collecting data from the BRBs was one of the most important tasks. Therefore, because the BRB yield displacements are small [~0.76 mm (0.03 in.)], four linear potentiometers (LPs) were used in each BRB to measure the displacement of BRBs, two at each end. Additionally, each BRB had two string potentiometers (SPs) to measure large displacements between the gusset plates where BRBs were connected, and two to six strain gauges (SGs) were installed on the BRB endplates to measure axial and bending strains in the endplates and used to also monitor the integrity of the BRB (i.e., its ability to resist axial forces as described subsequently).

The force in the BRBs were approximated from strain gauges installed on the BRBs end plates outside the casings where the material remained elastic along the test. This location was obtained from numerical analysis, and load testing of individual BRBs confirmed that gauges remain in the elastic range and allowed to obtain (by calibration) BRB forces. A minimum of eight instruments were used per BRB. For the remaining structure; several SPs, LPs, SGs, and accelerometers were used to provide a relatively comprehensive measurement of its behavior. A total of 156 instruments were used.

To obtain ground motions representative of the design level, four long-duration and strong ground motions were selected to be used as seeds for a spectral matching process. For scaling, the original design spectrum (Fig. 2) was adjusted such that the strength of BRBs required per the proposed design procedure was similar to the strength of the BRBs delivered to SEESL. Additionally, five motions were selected and amplitude-scaled to generate the largest possible deformation demands in the BRBs. These motions were representative of near-fault motions, far-field motions (FF), motions with pulses, and motions in soft soils. Finally, as a contingency in case the BRBs could not be failed under the previous motions, two extreme motions were selected and used as the input of both shake tables. Ground motions used are presented in Table 1.

In addition, a motion used to represent thermal expansion was obtained from the numerical model of the prototype subject to 75 years of temperature variations. The temperature record from Memphis, Tennessee, was used as the input, which was previously studied by Wei and Bruneau (2018). For this sequence, one table was kept fixed, and the other shake table moved in the longitudinal direction.

Testing

Fig. 8 shows the specimen set up on top of both shake tables.

In the bridge specimen, BRBs were installed in two different configurations. Both have BRBs in the transverse and longitudinal direction. In the longitudinal direction of Configuration I, the two BRBs are almost horizontal, as shown in Fig. 9. In the longitudinal direction of Configuration II, the two BRBs are at an angle of 30° from the horizontal, as shown in Fig. 10. In both configurations, in the longitudinal direction, the connection of one BRB was bolted and the other was pinned, and in the transverse direction, all BRBs

Table 1. Base ground motions for different motion testing groups

Group	Motion name of the base record	Data source
Spectral matched motions	Imperial Valley	PEER (2006) ground motion 169
	Chi-Chi	PEER ground motion 1244
	Manjin, Iran	PEER ground motion 1633
	Synthetic	Created using SeismoArtif (Version 2021)
Motions from different sources	Northridge–FF	PEER ground motion 953
	El Centro	PEER ground motion 6
	Kobe–pulse	PEER ground motion 1114
	Kobe–FF	PEER ground motion 1116
	Puebla, Mexico	Mexico, Roma Norte 2017, CIRES (2005)
Motions assuming rigid piers	Puebla, Mexico	Mexico, Roma Norte 2017, CIRES
	Pedernales, Ecuador	Ecuador, Portoviejo 2016, RENAC (Singaucho et al. 2016)

Note: PEER = Pacific Earthquake Engineering Research Center; CIRES = Centro de Instrumentación y Registro Sísmico, A. C.; and RENAC = Red Nacional de Acelerógrafos.

Fig. 8. Specimen set up on top of the two shake tables.

(a) (b)

Fig. 9. Specimen with BRBs and instrumentation for Configuration I: (a) transverse BRB in the west end; and (b) longitudinal BRB.

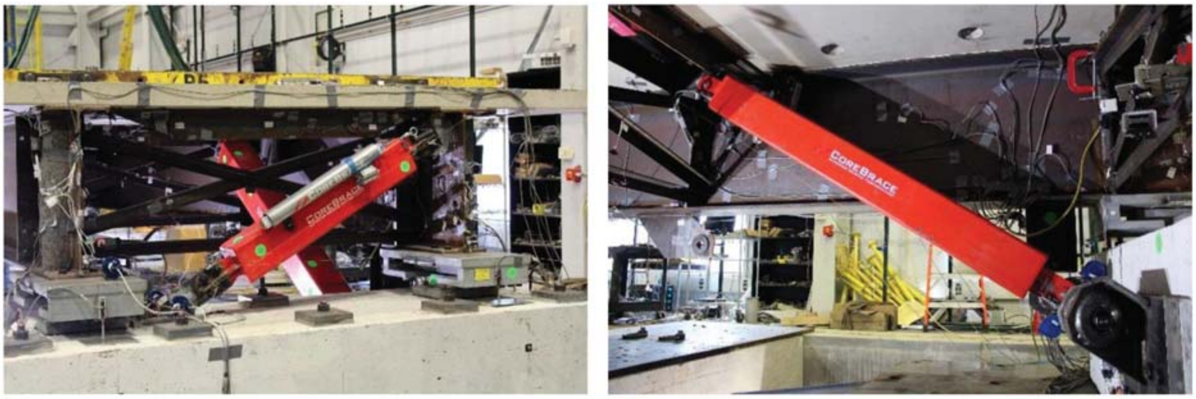

(a) (b)

Fig. 10. Specimen with BRBs and instrumentation for Configuration II: (a) transverse BRB in the west end; and (b) longitudinal BRB.

had bolted connections, as shown in Fig. 11. Some results from the data analysis are presented in the next sections.

Fidelity of the Movement

The fidelity of shake-table movement was analyzed by comparing the ratio of output to input pseudospectra acceleration. Because there was no significant sliding observed between the shake table and the concrete block, the accelerations obtained from accelerometers on the concrete block were considered to be the same as the accelerations of the shake table for this purpose. Therefore, these were used to calculate the pseudoacceleration spectra obtained from the shake-table movement and compare them with the spectra corresponding to the input control signal. The table control parameters were originally tuned after installing the reaction blocks and before installing the specimen, but that these parameters were continuously adjusted during the test to improve this fidelity as the experimental program progressed. The ratio of the output to the input spectra was calculated over the period range of 0 to 0.6 s (equal to 0 to 2 s in the prototype). These ratios were then studied statistically.

Fig. 12 shows the mean and the mean $\pm$ one standard deviation of these ratios for selected motions when fidelity was improved after application of a number of ground motions. A value equal to 1.0 implies perfect fidelity, where values above and below reflect over- and undershooting of the target acceleration spectra. Before adjustments, for some motions and depending on the period, the ratio varied from 0.6 to 3, but generally the average was above one, particularly after fidelity was improved, as shown in Fig. 12.

Configuration I

Fig. 13 shows hysteretic loops for all BRBs in Configuration I for ground motions representing the design spectrum, and Fig. 14 shows a preliminary hysteretic loop of one failed BRB.

When comparing the force obtained from strain gauges with the inertia force obtained from accelerometers, both are in good agreement, as shown in Fig. 15. In this configuration, one BRB in the transverse direction failed after completing testing of the set of all ground motions representing the design level, the history representing temperature cycles, and a few of the stronger ground motions. Two other BRBs failed after testing all motions. Here, failure is defined as fracture of the core due to low-cycle fatigue, which is the known ultimate limit state of well-designed BRBs (Li et al. 2022). The maximum BRB demands obtained are summarized in Table 2.

Demands from motions at the design level (i.e., spectral matched motions) are detailed in Table 3 and are compared with demands expected from numerical analysis. For these motions, in general, demands from numerical analysis were larger than those obtained from experiment. From instrumentation, it was verified that this reduction in demand was not associated with sliding in bolted connections, which was not observed. This reduction is consistent with the fact that it was also observed (not shown here) that

J. Struct. Eng., 2024, 150(7): 04024063

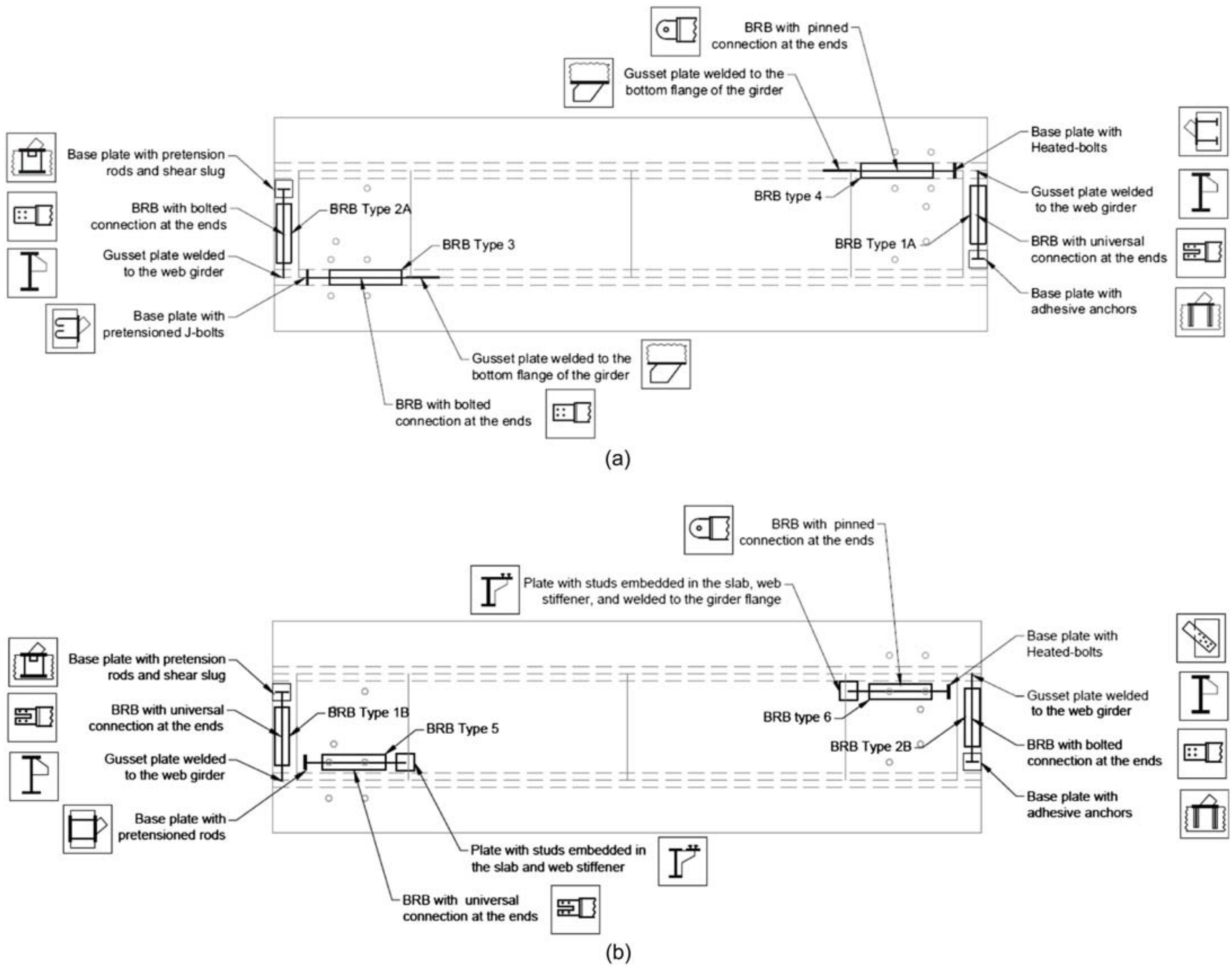

Fig. 11. Location of different details in plan view of bridge specimen: (a) Configuration I; and (b) Configuration II.

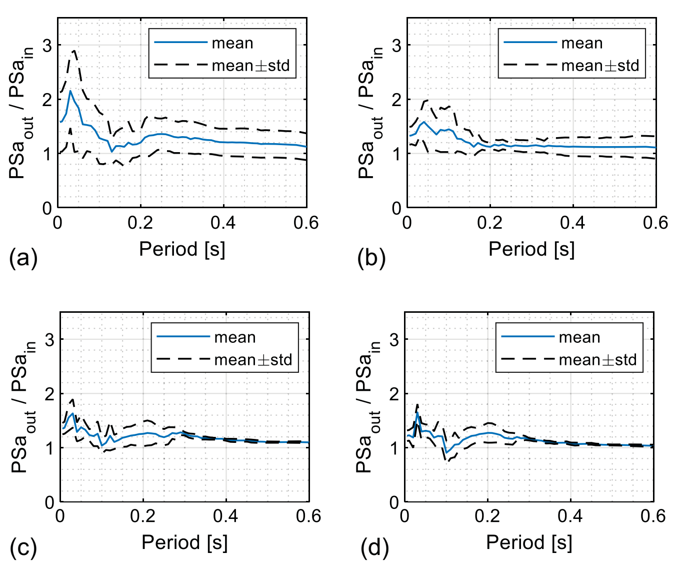

Fig. 12. Ratio of output to input spectral accelerations: (a) west table longitudinal; (b) east table longitudinal; (c) west table transverse; and (d) east table transverse.

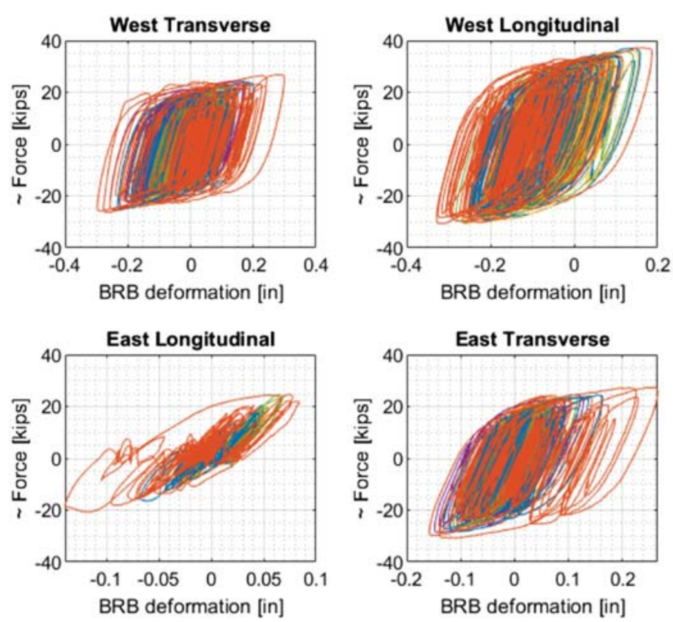

Fig. 13. BRB hysteretic loops for all spectral matched motions for Configuration I. 1 kip = 4.448 kN, and 1 in. = 25.4 cm.

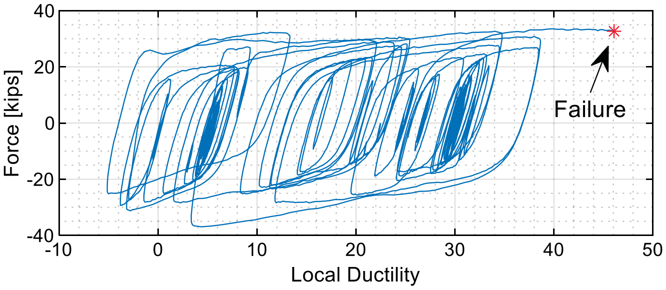

Fig. 14. Preliminary hysteretic loop of a BRB from a few ground motions before its failure. This is truncated data; for clarity, the hysteretic curves corresponding to all the ground motions tests applied to this BRB are not all included in this figure. 1 kip = 4.448 kN.

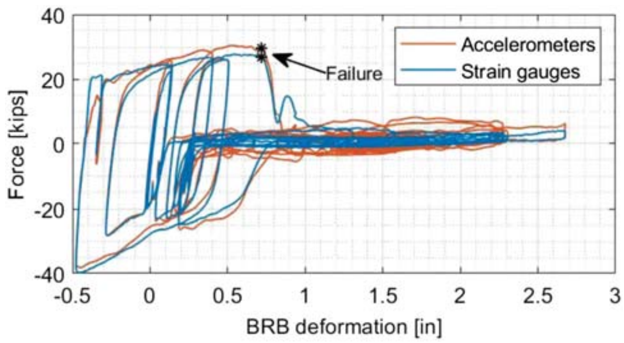

Fig. 15. West transverse BRB hysteretic loops for the failure step (Step 95) with forces approximated from strain gauges and inertia force. 1 kip = 4.448 kN, and 1 in. = 25.4 cm.

the backbone curve of the BRB model used in numerical analysis was contained inside the envelope of the experimentally obtained hysteretic curves.

Fig. 16 shows cumulative BRB residual displacements, where each test of the specimen is referred to as a test step. By the 70th test step, all design-level ground motions had been applied, and residual displacements were found to be negligible. Residual displacements were generally small after each individual earthquake, and the maximum residual displacements before failure remained less than 20 times the BRB yield deformation for cases where BRBs reached core ductilities of up to 30. Fig. 17 shows that for each of the ground motions tested, cumulative plastic deformation demands were generally less than 200 times the BRB yield deformation (the two peaks in the figure for steps smaller than 70 represents motions scaled 20% to 25% above the design level), except for one earthquake (namely, the 2017 Puebla, Mexico, earthquake scaled to 2.25 times its original record), where the cumulative plastic deformation demand was approximately 400 times the BRB yield deformation. Results also showed that deformations due to temperature cycles induced smaller fatigue demands in BRBs than earthquakes. Finally, none of the various BRB connections used showed instability during testing and maximum demands, and the BRBs yielded in compression are presented in Table 4.

Configuration II

This configuration performed similarly to Configuration I. In comparison with Configuration I, this configuration was tested twice for ground motions representing the design level. The first time,

Table 2. Summary of maximum BRB demands for Configuration I

Description	WT	WL	EL	ET
BRB number	2a	3a	4a	1a
Maximum deformation (in.)	0.72	1.94	1.55	1.22
Minimum deformation (in.)	−0.77	−0.84	−1.59	−0.16
Maximum deformation amplitude (in.)	1.49	2.78	3.14	1.38
Maximum core strain (%)	3.4	5.5	4.4	6.3
Minimum core strain (%)	−3.6	−2.4	−4.5	−0.8
Amplitude core strain (%)	7.0	7.9	8.9	7.1
Amplitude normalized by core yielding strain	53	60	68	54
Cumulative inelastic deformation	1,332	1,793	671	664
Maximum force (tension) (kip)	31	46	36	33
Maximum force (compression) (kip)	40	46	40	35
Ω	1.63	2.01	1.89	1.73
$\Omega\beta$	2.10	2.01	2.01	1.84
Status	Failed	Failed	Failed	—

Note: WT = west transverse BRB; WL = west longitudinal BRB; ET = east longitudinal BRB; and ET = east transverse BRB. 1 in. = 25.4 mm, and 1 kip = 4.448 kN.

Table 3. Mean deformation in BRBs from NL-RHA (in.) compared with experimental values for spectral matched ground motions

BRB	WT	WL	EL	ET
Numerical model	0.17	0.29	0.07	0.22
Experiment	0.19	0.22	0.06	0.14

Note: WL = west longitudinal BRB; EL = east longitudinal BRB; WT = west transverse BRB; and ET = east transverse BRB. 1 in. = 25.4 mm.

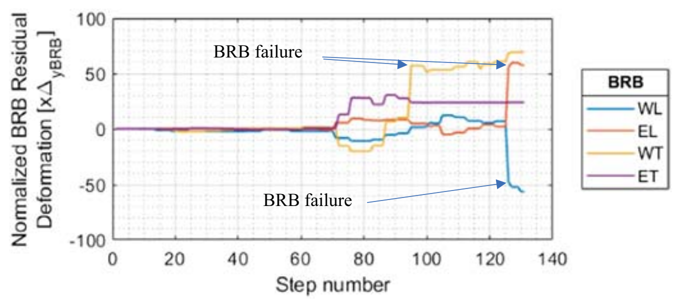

Fig. 16. Normalized residual BRB deformations. WL = west longitudinal BRB, EL = east longitudinal BRB, WT = west transverse BRB, and ET = east transverse BRB.

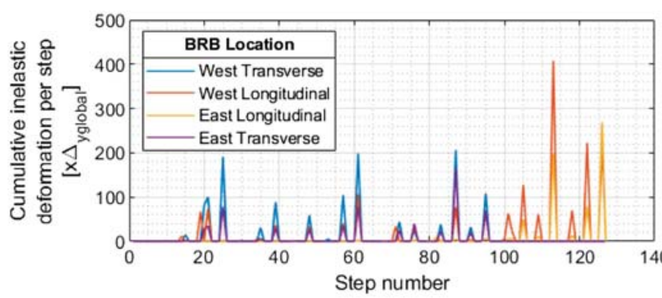

Fig. 17. BRB cumulative inelastic deformation per step for Configuration I.

Table 4. Maximum connections demands in Configuration I when BRBs were yielding in compression

Description	BRB location WT	WL	EL	ET
Horizontal out-of-plane displacement (in.)	0.95	2.1	1.3	0.08
Distance between hinges for vertical rotation (in.)	56	74	69	57
Horizontal angle ($\times 10^{-2}$ rad)	1.7	2.8	1.9	1.4
Horizontal angle (degrees)	0.97	1.60	1.08	0.80
Vertical component displacement (in.)	—	—	—	0.57
Distance between hinges for horizontal rotation (in.)	—	—	—	42
Vertical angle ($\times 10^{-2}$ rad)	—	—	—	1.26
Vertical angle (degrees)	—	—	—	0.7

Note: WN = west north BRB; WS = west south BRB; EN = east north BRB; and ES = east south BRB. 1 in = 25.4 mm.

Table 5. Mean apparent BRB deformation

Description	BRB location WT	WL	EL	ET
Analytical result for motions at 100%, no vertical (in.)	0.19	0.27	0.07	0.24
Experiment E08-E07 100%, with vertical (in.)	0.18	0.27	0.10	0.16
Experiment E01-E04 100%, no vertical (in.)	0.20	0.26	0.09	0.17
Ratio experimental to analytical, no vertical (in.)	1.05	0.96	1.29	0.71
Ratio experimental with vertical to without vertical (in.)	0.90	1.04	0.9	0.94

Note: 1 in. = 25.4 mm.

only the two horizontal components of ground excitation were considered, and the second time, vertical components were also included. Comparison of numerical and experimental demands are presented in Table 5. After one BRB failed, it was replaced in Step 68 by the BRB 1a (which is weaker than the original BRB used) that did not fail in Configuration I before resuming the test.

Cumulative inelastic deformations are shown in Fig. 18. Generally, no single history used generated more than 200 times the global yield deformation (the largest was 190), with exception of the 2017 Puebla, Mexico, motion at 100% scale (which represent the original motion scaled 3.95 times) when assuming rigid piers, and except for the results for the replaced BRB (west transverse from Step 68 to Step 77).

Maximum demands in connections while the BRB was yielding in compression are presented in Table 6. Finally, the maximum demands in BRBs (without considering the replaced BRB) are presented in Table 7.

Comparison with Numerical Analysis

As mentioned previously, BRBs were designed based on an ELF design procedure presented by Carrion-Cabrera and Bruneau (2023); this procedure was derived based on results of a simplified nonlinear numerical model presented by Carrion-Cabrera and Bruneau (2022a, b). This numerical model was also used here during the design of the prototype to better estimate demands and to

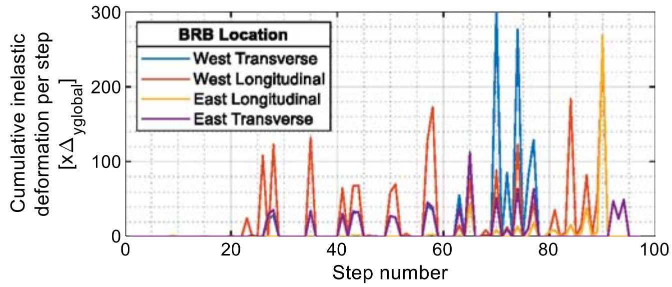

Fig. 18. Cumulative inelastic deformation in each step for Configuration II.

Table 6. Maximum connection demands for Configuration II when BRBs were yielding in compression

Description	BRB location WT	WL	EL	ET
Maximum step considered	65	90	90	97
Horizontal out-of-plane displacement (in.)	0.70	3.48	2.13	1.05
Distance between hinges for vertical rotation (in.)	56.00	73.75	76.00	55.75
Horizontal angle ($\times 10^{-2}$ rad)	1.25	5.20	2.80	1.88
Horizontal angle (degrees)	0.72	2.98	1.60	1.08
Bending strain due to horizontal displacement, μ (in./in.)	900	1,400	1,200	730
Vertical component displacement (in.)	0.25	0.76	—	0.45
Distance between hinges for horizontal rotation (in.)	42.00	53.75	—	55.75
Vertical angle ($\times 10^{-2}$ rad)	0.60	1.40	—	0.81
Vertical angle (degrees)	0.30	0.81	—	0.46
Strain due to vertical displacement (in./in.)	1,000	1,800	—	—

Note: WN = west north BRB; WS = west south BRB; EN = east north BRB; and ES = east south BRB. 1 in. = 25.4 mm.

generate inputs to the shake table. Here, the numerical response in the longitudinal direction of the specimen tested (which was the missing part needed to fully implement the bidirectional ductile end diaphragm) is compared with experimental results to validate the model, and therefore, to verify the effectiveness of the design procedure. In this process, BRB deformation demands obtained numerically from the simple nonlinear models are presented in terms of BRB global ductility. These are compared with the apparent BRB deformation demands obtained from the test of Configurations I and II for BRBs aligned with the longitudinal direction and only for ground motions tested at 100% of the design basis.

Fig. 19 shows the ratio of numerical-to-experimental demand and as a function of the global ductility demand obtained numerically. The figure presents results statistically in bins of width equal to units of ductility demand and represented by boxplots, where it is shown that the median (represented by the dot at the center of the box) is close to one and generally less than one. For a ductility demand in one BRB equal to five obtained from nonlinear response history analysis (NL-RHA), where the BRB was designed for a target ductility equal to 10 (recall that not all BRBs along the bridge

Table 7. Summary of extreme BRB demands for Configuration II original BRBs

Description	WT	WL	EL	ET
BRB number	1b	5a	6a	2b
Maximum deformation (in.)	0.50	1.10	0.35	0.93
Minimum deformation (in.)	−0.43	−0.85	−1.52	−0.19
Max deformation amplitude (in.)	0.93	1.95	1.87	1.13
Maximum core strain (%)	2.58	3.82	1.16	4.40
Minimum core strain (%)	−2.21	−2.95	−4.97	−0.90
Amplitude core strain (%)	4.79	6.77	6.13	5.30
Expected core yielding strain (%)	0.18	0.13	0.13	0.18
Normalized amplitude by core yielding strain	26.2	51.6	46.7	29.1
Cumulative inelastic deformation	477	2,047	456	817
~Maximum force (tension) (kip)	37.7	43.5	35.1	46.1
~Maximum force (compression) (kip)	47.6	59.1	58.2	40.7
ω	1.42	1.63	1.59	1.74
$\omega\beta$	1.80	2.21	2.63	1.54
Final status	Failed	Failed	Failed	—

Note: WN = west north BRB; WS = west south BRB; EN = east north BRB; and ES = east south BRB. 1 in. = 25.4 mm, and 1 kip = 4.448 kN.

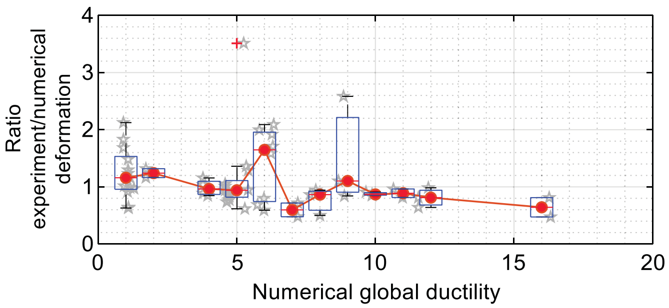

Fig. 19. Comparison between BRB demands from numerical analysis and BRB demands from testing of Configuration I and II and only for BRBs in the longitudinal direction, and statistical analysis of demands using boxplots.

will reach the target ductility), a ratio of four in the figure implies that the BRB would deform up to a ductility of 20, which is within the range of deformation that a BRB design for a target ductility of 10 is capable of developing (as required by the AISC qualification test protocol). Fig. 19 also shows that for expected ductilities equal to 10 and larger, the ratio between expected and experimental deformations are less than one. These results validate the fact that the simplified numerical models can give reasonable prediction of behavior and therefore validate the design procedure that resulted from analyses with those models.

Conclusions

Shake-table experiments were conducted to evaluate and validate the behavior of bidirectional ductile end diaphragms having BRBs as the energy-dissipating elements. Two different BRB configurations were used at the ends of the bridge span tested. Overall, the results obtained for Configurations I and II indicated that the design procedure proposed is acceptable given its simplicity, and is conservative because it led to a design that resulted in predicted demands slightly larger than those observed during testing. Furthermore, by increasing the severity of the ground excitations to push the specimen to failure, it was demonstrated that the BRBs could develop core ductilities greater than 20.

Moreover, it was observed that the temperature effects are small in comparison with demands imposed by seismic motions for this particular configuration/design. The fact that temperature effects did not control the design performance was achieved by an adequate selection of the length of the BRB. Based on the numerical analysis and experimental results, if the deformation amplitude demanded by temperature cycles is in the range of two times the BRB global yield displacement, the temperature cycles over the 75-year service life of the bridge will not have any negative impact on the seismic performance of the bridge.

Regarding the various types of connections used, they all provided adequate support for the BRBs in terms of strength (transferring forces) and stability (providing satisfactory development of rotation capabilities under full loading). Because they all performed as intended by accommodating the 3D relative displacements that develop during the seismic response, this offers many different connection options to bridge engineers.

Appendix. Equivalent Lateral Force Method

Design requirements for already present in the AASHTO *Guide Specifications for LRFD Seismic Design* (AASHTO 2011) were followed to design the BRBs to resist seismic excitations transversally to the axis of bridges. The BRBs to resist seismic excitation longitudinally to the axis of bridges (complementing AASHTO and thus making possible a complete bidirectional ductile end diaphragm concept) were designed per the ELF design procedure as follows:

1. Ductile diaphragms designed with buckling restrained braces connecting spans to abutments and piers for simply supported spans supported by slider bearings were designed using forces, F_i, determined by the following equivalent lateral force method as follows:

$$F_i = \frac{W\,Sa(T)}{R}\frac{m_i\phi(x_i)}{\sum_{j=1}^{N_{\text{span}}} m_j\phi(x_j)}$$

where i = integer representing location the ith span and is taken as $(i+0.5)$ when representing location of the pier cap mass in between the ith and $(i+1)$th span; m_i = mass of the ith element; W = total weight of the bridge; R = response modification factor; $Sa(T)$ = spectral acceleration in units of gravity; N_{span} = number of spans; and x = normalized distance that represent the position of the center of mass of each span along the length of the bridge, set at zero at midlength of the bridge and to $+1$ and -1 at opposite bridge ends, and is defined

$$x = 1 - 2\frac{i-1}{N_{\text{span}}-1}$$

2. Additional parameters are defined as follows:

$$\gamma = \frac{T_p}{T_{\text{SDOF}}}$$

$$\lambda = 1 - \frac{8}{\gamma^2 + 8}$$

$$\eta = \frac{T}{T_{\mathrm{SDOF}}} = 1 + 0.4 \cdot \lambda \cdot N_{\mathrm{span}}$$

where

$$T_p = 2\pi\sqrt{\frac{M_{\mathrm{span}}}{K_{\mathrm{pier}}}}$$

and T_{SDOF} = period of a one-span bridge with mass equal to the median span mass of the multispan bridge and designed to reach the target ductility and target maximum deformation in BRBs.

3. The approximate fundamental period of the structure, T (s), was determined from the following equation:

$$T = \eta \cdot T_{\mathrm{SDOF}}$$

4. The equivalent mode shape, ϕ, was determined from the following equation:

$$\phi(x) = 1 + y(x, k_1) - y(x, k_2)$$

where

$$y(x,k) = 1 - \left(0.6 + \frac{\mu}{100}\right)\left[1 - \left(1 - \frac{|x|^{\frac{1}{k}}}{1.1}\right)^k\right]$$

$$k_1 = 4 \cdot \lambda \leq 0.15(10 + \mu)(1 - 0.7^{N_{\mathrm{span}}-2})$$

$$k_2 = 0.06 \cdot (\gamma - 1) > 0$$

and μ = target ductility expected in BRBs. Here, μ was taken between 5 and 10.

5. The R value was calculated using the following equations:

$$R(T) = \begin{cases} \left(\frac{\mu}{\alpha_u \gamma_\mu} - 1\right)\frac{T}{1.25T_s} + 1 & \text{if } T < 1.25T_s \\ \frac{\mu}{\alpha_u \gamma_\mu} & \text{otherwise} \end{cases}$$

where

$$\alpha_u = 0.06\mu_{\mathrm{SDOF}} + 0.7 \geq 1 \quad \text{if } \mu \leq 10$$

$$\gamma_\mu = 2\eta - 1 \leq 2.0$$

T_{SDOF} was calculated assuming $\eta = 1$.

6. Both group of BRBs connected on each side of the pier caps were set to have the same group strength.
7. The buckling restrained brace cross-section area was not taken be smaller than half the cross-section area calculated for the same bridge considering infinitely rigid piers.

The adequacy of this design procedure was investigated and verified by Carrion-Cabrera and Bruneau (2023).

Data Availability Statement

Some or all data, models, or code that support the findings of this study are available from the corresponding author upon reasonable request.

Acknowledgments

This study was sponsored by the Transportation Research Board of the National Academies under the TRB-IDEA Program (NCHRP-215). The Fulbright program, SENESCYT Ecuador, and the University of Buffalo, are also acknowledged for their financial support through a scholarship to Dr. Homero Carrion Cabrera. This research was also made possible thanks to the significant donations of material and in-kind donations from the American Institute of Steel Construction, the High Industries Inc. companies (High Steel, High Concrete, and High Transit), CoreBrace LLC, and RJ Watson Inc. However, any opinions, findings, conclusions, and recommendations presented are those of the authors and do not necessarily reflect the views of the sponsors.

References

AASHTO. 2011. *AASHTO guide specifications for LRFD seismic bridge design*. 2nd ed. Washington, DC: AASHTO.

AASHTO. 2017. *AASHTO LRFD bridge design specifications*. 8th ed. Washington, DC: AASHTO.

ACI (American Concrete Institute). 2019. *Building code requirements for structural concrete (ACI 318-19): An ACI standard: Commentary on building code requirements for structural concrete*. ACI 318R-19. Farmington Hills, MI: ACI.

AISC (American Institute of Steel Construction). 2016. *Specification for structural steel buildings*. ANSI/AISC 360-16. Chicago: AISC.

AISC (American Institute of Steel Construction). 2022. *Seismic provisions for structural steel buildings*. ANSI/AISC 341-22. Chicago: AISC.

Alfawakhiri, F., and M. Bruneau. 2001. "Local versus global ductility demands in simple bridges." *J. Struct. Eng.* 127 (5): 554–560. https://doi.org/10.1061/(ASCE)0733-9445(2001)127:5(554).

Carden, L. P., A. M. Itani, and I. G. Buckle. 2006. "Seismic performance of steel girder bridges with ductile cross frames using buckling-restrained braces." *J. Struct. Eng.* 132 (3): 338–345. https://doi.org/10.1061/(ASCE)0733-9445(2006)132:3(338).

Carden, L. P., A. M. Itani, and I. G. Buckle. 2008. *Seismic performance of steel girder bridge superstructures with ductile end cross frames and seismic isolators*. Rep. No. MCEER-08-0002. New York: Multidisciplinary Center for Earthquake Engineering Research.

Carrion-Cabrera, H., and M. Bruneau. 2022a. "Longitudinal-direction design of buckling restrained braces implemented to achieve resilient multi-span bridges." In *Proc., Institution of Civil Engineers-Bridge Engineering*, 1–28. London: Institution of Civil Engineers. https://doi.org/10.1680/jbren.21.00097.

Carrion-Cabrera, H., and M. Bruneau. 2022b. "Seismic response of regular multi-span bridges having buckling-restrained braces in their longitudinal direction." *Eng. Struct.* 259 (May): 114127. https://doi.org/10.1016/j.engstruct.2022.114127.

Carrion-Cabrera, H., and M. Bruneau. 2023. "Equivalent lateral force design method for longitudinal buckling restrained braces in bi-directional ductile diaphragms." *ASCE J. Struct. Eng.* 150 (3): 04024003. https://doi.org/10.1061/JSENDH.STENG-12846.

Celik, O. C., and M. Bruneau. 2009. "Seismic behavior of bidirectional-resistant ductile end diaphragms with buckling restrained braces in straight steel bridges." *Eng. Struct.* 31 (2): 380–393. https://doi.org/10.1016/j.engstruct.2008.08.013.

CIRES (Centro de Instrumentación y Registro Sísmico). 2005. "Centro de Instrumentación y Registro Sísmico, México." Accessed November 2, 2017. http://www.cires.org.mx/.

CoreBrace. 2020. "Vancouver city hall." Accessed June 1, 2020. https://www.corebrace.com/project/vancouver-city-hall/.

CoreBrace. 2021. "Vincent thomas bridge." Accessed January 2, 2021. https://corebrace.com/project/vincent-thomas-bridge-seismic-braces/.

Enke, D. L., C. Tirasirichai, and R. Luna. 2008. "Estimation of earthquake loss due to bridge damage in the St. Louis metropolitan area. II: Indirect losses." *Nat. Hazards Rev.* 9 (1): 12–19. https://doi.org/10.1061/(ASCE)1527-6988(2008)9:1(12).

Harris, H. G., and G. Sabnis. 1999. *Structural modeling and experimental techniques*. Boca Raton, FL: CRC Press.

Ingham, T., S. Rodriguez, and M. Nader. 1997. "Nonlinear analysis of the Vincent Thomas Bridge for seismic retrofit." *Comput. Struct.* 64 (5–6): 1221–1238. https://doi.org/10.1016/S0045-7949(97)00031-X.

Kanaji, H., N. Hamada, T. Ishibashi, M. Amako, and T. Oryu. 2005. "Design and performance tests of buckling restrained braces for seismic retrofit of a long-span bridge." In *Proc., 21th US–Japan Bridge Engineering Workshop Panel on Wind and Seismic Effects*. Tsukuba, Japan: Scrib.

Lanning, J., G. Benzoni, and C.-M. Uang. 2016a. "Using buckling-restrained braces on long-span bridges. I: Full-scale testing and design implications." *J. Bridge Eng.* 21 (5): 04016001. https://doi.org/10.1061/(ASCE)BE.1943-5592.0000781.

Lanning, J., G. Benzoni, and C.-M. Uang. 2016b. "Using buckling-restrained braces on long-span bridges. II: Feasibility and development of a near-fault loading protocol." *J. Bridge Eng.* 21 (5): 04016002. https://doi.org/10.1061/(ASCE)BE.1943-5592.0000804.

Li, C.-H., Z. Vidmar, B. Saxey, M. Reynolds, and C.-M. Uang. 2022. "A procedure for assessing low-cycle fatigue life of buckling-restrained braces." *J. Struct. Eng.* 148 (2): 04021259. https://doi.org/10.1061/(ASCE)ST.1943-541X.0003237.

MacRae, G., C.-L. Lee, S. Vazquez-Coluga, J. Cui, S. Alizadeh, and L.-J. Jia. 2021. "BRB system stability considering frame out-of-plane loading and deformation zone." *Bull. N Z Soc. Earthquake Eng.* 54 (1): 31–39. https://doi.org/10.5459/bnzsee.54.1.31-39.

PEER (Pacific Earthquake Engineering Research). 2006. *PEER NGA database*. Berkeley, CA: PEER.

Singaucho, J. C., A. Laurendeau, C. Viracucha, and M. Ruiz. 2016. "Observaciones del sismo del 16 de Abril de 2016 de magnitud Mw 7.8, Intensidades y Aceleraciones." Accessed June 1, 2020. https://www.igepn.edu.ec/servicios/noticias/1324-informe-sismico-especial-n-18-2016.

Takeuchi, T., H. Ozaki, R. Matsui, and F. Sutcu. 2014. "Out-of-plane stability of buckling-restrained braces including moment transfer capacity." *Earthquake Eng. Struct. Dyn.* 43 (6): 851–869. https://doi.org/10.1002/eqe.2376.

Wei, X., and M. Bruneau. 2016. *Buckling restrained braces applications for superstructure and substructure protection in bridges*. Rep. No. MCEER-16-0009. New York: Multidisciplinary Center for Earthquake Engineering Research.

Wei, X., and M. Bruneau. 2018. "Experimental investigation of buckling restrained braces for bridge bidirectional ductile end diaphragms." *J. Struct. Eng.* 144 (6): 04018048. https://doi.org/10.1061/(ASCE)ST.1943-541X.0002042.

Zaboli, B., G. Clifton, and K. Cowie. 2018. "BRBF and CBF gusset plates: Out-of-plane stability design using a simplified notional load yield line (NLYL) method." *SESOC J.* 31 (1): 64.

Zahrai, S. M., and M. Bruneau. 1999a. "Cyclic testing of ductile end diaphragms for slab-on-girder steel bridges." *J. Struct. Eng.* 125 (9): 987–996. https://doi.org/10.1061/(ASCE)0733-9445(1999)125:9(987).

Zahrai, S. M., and M. Bruneau. 1999b. "Ductile end-diaphragms for seismic retrofit of slab-on-girder steel bridges." *J. Struct. Eng.* 125 (1): 71–80. https://doi.org/10.1061/(ASCE)0733-9445(1999)125:1(71).